ACS SENSORS

pubs.acs.org/acssensors

Article

InGaAs Membrane Waveguide: A Promising Platform for Monolithic Integrated Mid-Infrared Optical Gas Sensor

Kyoung Min Yoo, Jason Midkiff, Ali Rostamian, Chi-jui Chung, Hamed Dalir, and Ray T. Chen*

Cite This: *ACS Sens.* 2020, 5, 861−869

Read Online

ACCESS | Metrics & More | Article Recommendations | Supporting Information

ABSTRACT: Mid-infrared (mid-IR) absorption spectroscopy based on integrated photonic circuits has shown great promise in trace-gas sensing applications in which the mid-IR radiation directly interacts with the targeted analyte. In this paper, considering monolithic integrated circuits with quantum cascade lasers (QCLs) and quantum cascade detectors (QCDs), the InGaAs−InP platform is chosen to fabricate passive waveguide gas sensing devices. Fully suspended InGaAs waveguide devices with holey photonic crystal waveguides (HPCWs) and subwavelength grating cladding waveguides (SWWs) are designed and fabricated for mid-infrared sensing at $\lambda = 6.15\ \mu m$ in the low-index contrast InGaAs−InP platform. We experimentally detect 5 ppm ammonia with a 1 mm long suspended HPCW and separately with a 3 mm long suspended SWW, with propagation losses of 39.1 and 4.1 dB/cm, respectively. Furthermore, based on the Beer−Lambert infrared absorption law and the experimental results of discrete components, we estimated the minimum detectable gas concentration of 84 ppb from a QCL/QCD integrated SWW sensor. To the best of our knowledge, this is the first demonstration of suspended InGaAs membrane waveguides in the InGaAs−InP platform at such a long wavelength with gas sensing results. Also, this result emphasizes the advantage of SWWs to reduce the total transmission loss and the size of the fully integrated device's footprint by virtue of its low propagation loss and TM mode compatibility in comparison to HPCWs. This study enables the possibility of monolithic integration of quantum cascade devices with TM polarized characteristics and passive waveguide sensing devices for on-chip mid-IR absorption spectroscopy.

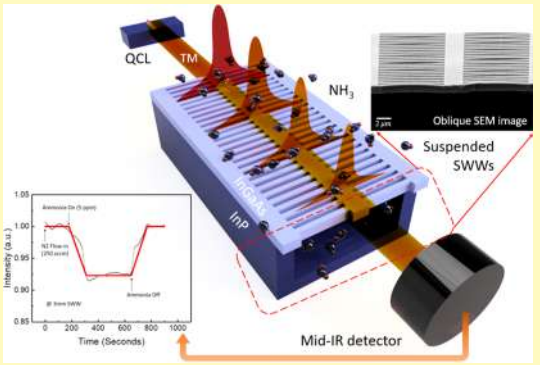

KEYWORDS: *mid-infrared, absorption spectroscopy, quantum cascade devices, subwavelength waveguides, photonic crystal waveguides, photonics integrated circuits, parts per billion, gas sensing*

Due to its distinctive features, mid-IR photonics research has incited a great interest for various applications in civilian, military, and security domains. Among them, mid-IR trace-gas sensing is a vigorously developing field with a wide range of applications based on molecular absorption spectroscopy and the fundamental vibrational−rotational transitions of chemical bonds in the wavelength range of 3−20 μm. Specifically, unlike the shorter-wavelength mid-IR band (1500−3500 cm^{-1}), the molecular fingerprint region (700−1500 cm^{-1}) contains many absorption bands related to bending and stretching of molecular skeleton modes (such as −C−C−, −C−O−, −C−N−, etc.) that allow unique identification of chemical compounds with high sensitivity and specificity.[1] Among the analytes, ammonia sensing applications have been developed to protect livestock animals and farmers, control automotive NH_3 emissions or chemical leaking, and perform breath analysis for medical diagnosis.[2]

Conventionally, most mid-IR trace-gas sensing systems have been developed around bulky gas cells and free-space optics based on cavity ring-down spectroscopy (CRDS),[3] tunable diode laser absorption spectroscopy (TDLAS),[4] Fourier transform infrared (FTIR) spectroscopy, or photoacoustic spectroscopy (PAS) methods.[5] Even though these systems can perform parts per billion (ppb) and even parts per trillion (ppt) sensitivities, they require bulky and expensive optical elements and sensitive beam alignments, which place constraints on their applications in the field, particularly for airborne or handheld platforms. Recently, mid-IR absorption spectroscopy based on integrated photonic circuits has shown great promise in the sense that it can eliminate the needs of bulky gas cells and free-space optical components. Specifically, monolithic integration of light sources and detectors with passive photonics devices is required to enable a compact trace-gas sensing system that is robust to vibrations and physical stress.[6−8,21] Here, QCLs have significantly affected the feasibility of integrated photonic circuits by providing narrow-

Received: January 24, 2020
Accepted: March 4, 2020
Published: March 4, 2020

https://dx.doi.org/10.1021/acssensors.0c00180
ACS Sens. 2020, 5, 861−869

band-tunable continuous-wave room-temperature emission source in the entire mid-IR spectral range of 3−11 μm.[9,10] However, a suitably wide mid- and far-IR bandwidth (3−15 μm) passive photonic waveguiding platform has not been demonstrated yet. In this paper, we experimentally study and demonstrate a passive waveguiding platform considering monolithic integrated circuits with QCLs.

To date, several low-loss material platforms for mid-IR photonic devices have been explored, such as silicon-on-insulator (SOI), silicon-on-sapphire (SOS), Ge, Ge-on-Si (GOS), Ge−GaAs, GaAs−AlGaAs, and InGaAs−InP, to cover the entire molecular fingerprint region from λ = 3 to 15 μm.[11−21] Among them, intrinsic $In_{0.53}Ga_{0.47}As$ and InP materials exhibit near-complete transparency across the entire molecular fingerprint region (λ = 3−15 μm)[22−24] and $In_{0.53}Ga_{0.47}As$/InP waveguides offer a well-established lattice-matched, very low defect density platform for low-loss integrated optical circuits in the λ = 3−15 μm wavelength range. Furthermore, only the $In_{0.53}Ga_{0.47}As$/InP platform allows monolithic epitaxial growth of QCL/QCDs and eliminates the expensive and low-yield wafer/chip bonding processes of the other systems. It also eliminates the need for intermediate adhesive layers such as SU8 (lossy at λ > 5 μm wavelength), silicon dioxide (lossy at λ > 3.7 μm),[12] or complex surface activation strategies in direct wafer-to-wafer bonding.[25] Targeting monolithic integration of QCL/QCDs and passive devices, we choose the $In_{0.53}Ga_{0.47}As$/InP platform to fabricate passive waveguide devices.

Another important consideration is the optical path length that can be accommodated on a lab-chip to enable sufficient absorbance of the mid-IR light by the sensed analyte. Previously, it has been demonstrated that slow-light-enhanced two-dimensional (2D) photonic crystal waveguides (PCW), slotted PCWs (SPCWs), and holey PCWs (HPCWs) can effectively reduce the optical absorption path length due to the slow-light effect and increase the light−matter interaction length by enhancing the in-plane evanescent optical mode overlap within the low-index etched holes of the photonic crystal lattice.[26−31] Our previous research elaborated that the peak electric field enhancement factor in the SPCWs was better than that for the HPCWs; on the other hand, the propagation losses for the HPCWs were 3× lower than those for the SPCWs.[29] In recent years, subwavelength grating waveguides, or subwavelength meta-material clad waveguides, defined by a periodic array of rectangular holes bordering a strip waveguide, have been proposed as effective ways to ameliorate the cladding limitations, when appropriate high-index core materials are available.[14−17,32−35] It is known that subwavelength gratings (SWGs) act as an effective homogeneous medium with a spatially averaged refractive index.[33] Moreover, as a subcategory of one-dimensional (1D) PCWs, it has been studied that SWG waveguides generate slow light by way of periodically modulated structures along the propagation direction with a higher group index than conventional strip waveguides.[32−35]

In this paper, we designed fully suspended InGaAs HPCWs and subwavelength grating cladding waveguides (SWWs) for sensing ammonia, which has a peak absorbance at λ = 6.15 μm, and finally detected ammonia using each of the two structures.

DEVICE DESIGN

As our final targeted device is based on the homogeneous integration between QCL/QCDs and passive waveguides beneath them, the epitaxial material structure for this work is chosen considering efficient light coupling between these components. In our previous research, we addressed and demonstrated all fundamental methodology and device integration steps, including monolithic epitaxial growth of the QCL/QCDs and compact integrated passive components' fabrication feasibility.[36−40] Several important remarks are described in the Supporting Information. Figure S1 shows the schematic of fully integrated monolithic sensors with QCL/QCDs and suspended waveguide passive sensing device; also, the cross-sectional SEM images of suspended HPCWs and SWWs are shown. With regard to the structure of QCL/QCDs and PRS, the epi structure comprises an InP substrate with 1.15 μm InGaAs waveguide core layer targeting λ = 6.15 μm operating devices.[37−39] Figure 1a,b shows a schematic of

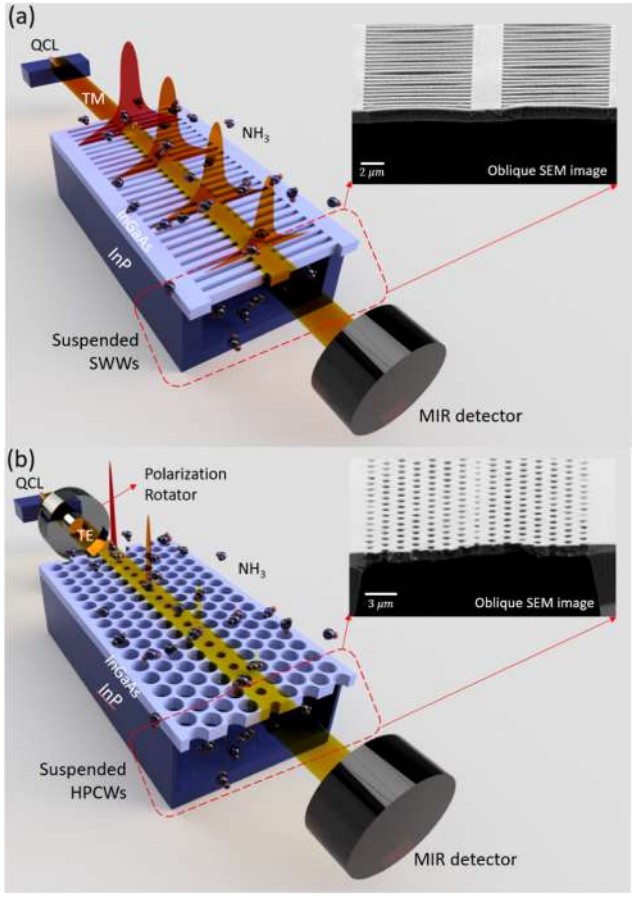

Figure 1. Schematic illustration of (a) suspended SWWs and (b) HPCWs' overall gas sensing operation and oblique cross-sectional SEM images of the real devices.

suspended SWW and HPCW devices that shows their structures and working characteristics with the corresponding SEM images. Detailed design principles for each device are described below.

Holey Photonic Crystal Waveguides (HPCWs). As described above, an HPCW shows high detection sensitivities due to the slow-light effect with a high group index value, and the TE mode is guided through the small hole defects in the center of the waveguide.[29] However, since the guided light in 2D PCWs is confined out of plane by total internal reflection (TIR), an index contrast of at least $\Delta n \sim 1.5$ is required between the core and the cladding to ensure an appreciable

https://dx.doi.org/10.1021/acssensors.0c00180
ACS Sens. 2020, 5, 861−869

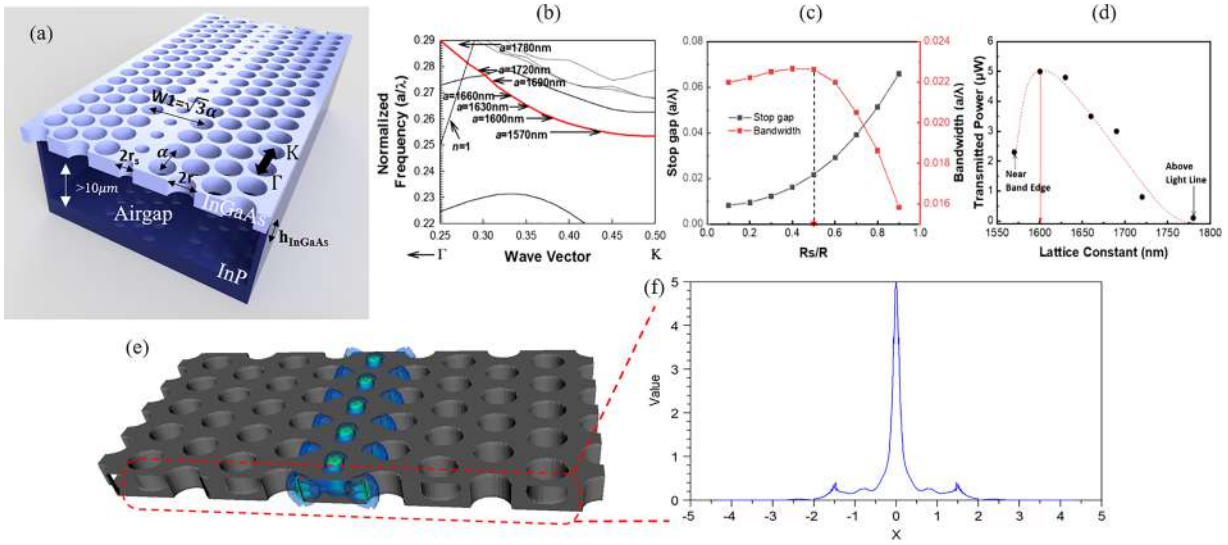

Figure 2. (a) 3D structure illustration of the fully suspended InGaAs HPCWs. (b) 3D plane-wave expansion (PWE) dispersion diagram of HPCWs in suspended membrane InGaAs in (a); devices were fabricated with various lattice constants "α" to probe the guided mode (red) using a single-wavelength external source at λ = 6.15 μm for optical characterization. (c) Bandwidth and stop gap variations versus r_s/r ratio. (d) Optical transmission characteristics versus various lattice constants with fixed r_s/r = 0.5 ratio; the highest transmitted power is achieved with α = 1600 nm. (e) 3D electric field intensity profile of the propagating slow-light-guided mode in (b). (f) Cross section of the electric field intensity profile in (e) taken on the red dashed plane, at the center of the slab through the small air holes in the center of the HPCW.

band gap for guiding slow light. In the InGaAs−InP material platform, the refractive indices are $n_{In0.53Ga0.47As} \cong 3.41$ and $n_{InP} \cong 3.09$ at λ = 6.15 μm, which are not enough to get TIR confinement between the core and the substrate; we therefore etch away the InP substrate to build suspended membrane waveguides to ensure $\Delta n \sim 2.4$ to assure slow-light PC guiding. The mode profiles propagating in the unsuspended and suspended InGaAs HPCWs in Figure S2a,b show the necessity of suspension of the waveguides in the low-index contrast InGaAs−InP platform. Moreover, suspended structures allow gas flow throughout the etched regions, giving more overlap with the optical mode.

A three-dimensional schematic of an InGaAs HPCWs membrane is shown in Figure 2a; the HPCW device comprises a W1 PCW with a single missing row of holes along the Γ−K direction in a hexagonal lattice of air holes in InGaAs with lattice constant α. In the center of the PCW, a row of smaller holes with radius $r_s = 0.5r$ is placed, where $r = 0.315\alpha$ is the radius of the holes in the bulk lattice; W1 indicates that the width of the PCW is $\sqrt{3}\alpha$. At λ = 6.15 μm, a single fundamental TE polarized mode is allowed in a waveguide with height h_{InGaAs} = 1.15 μm with air cladding. Figure 2b shows the simulated dispersion diagram of a suspended InGaAs HPCWs membrane. The dispersion diagram shows the guided mode (red line in Figure 2b) separated from the dielectric band by a stop gap. The light line for air (n = 1) is superimposed. We plotted the group index (n_g) versus wavelength in Figure S3. The optimized HPCW structure was designed to ensure a large guiding bandwidth for the propagating PCW guided mode as well as a large electric field overlap with the analyte. It is also necessary to ensure the existence of a sufficiently wide stop gap to enable a more accurate determination of the slow-light-guiding transmission regime of the guided mode. Figure 2c plots the guided mode bandwidth below the air light line and the width of the stop gap between the guided mode and the dielectric band in terms of normalized frequency (α/λ), as a function of the radius of the small holes, r_s. To ensure both good coupling to and propagation via the HPCW-guided mode, wide enough bandwidth and stop gap are required. The HPCW-guided mode bandwidth however falls off rapidly with increasing r_s. Hence, we chose r_s/r = 0.5, which has the maximum bandwidth point with positive stop gap value as our optimized design. Since the devices were to be characterized using a single-wavelength external source at λ = 6.15 μm, several 1 mm long devices were made with increasing lattice constants to probe the guided mode dispersion diagram from the stop band edge to above the air light line. Optical transmission measurements in Figure 2d show the variation in transmitted power as a function of lattice constant with fixed r_s/r = 0.5. The Group index of the guided mode is maximum at the band edge and decreases with increasing lattice constant farther from the band edge. As a result, transmitted power increases with increasing lattice constant away from the band edge.[30] However, the propagation loss is also increased as the light line is approached, so the total transmitted power is reduced when the lattice constant increases high.[31] We experimentally found the maximum transmitted power 5 μW from the HPCW device with lattice constant α = 1600 nm. Accordingly, we choose $r_s = 0.5r$, $r = 0.315\alpha$, and α = 1600 nm at λ = 6.15 μm as our optimized design, considering the above design constraints. The group index value extracted from the dispersion diagram (Figure S3) at λ = 6.15 μm is n_g = 39.3. The 3D electric field intensity profile of the propagating slow-light mode is shown in Figure 2e. Figure 2f is a two-dimensional (2D) cross section of the field intensity profile in Figure 2e, which is taken through the center of a small hole of the HPCW. The cross-sectional profile shows approximately 5 times enhancement of the peak electric field intensity in the small holes, and the percentage of electric field overlap with the analyte is approximately 12%.

Subwavelength Grating Cladding Waveguides (SWWs). We designed the suspended InGaAs SWWs, which have the suspended InGaAs strip defined between two SWG meta-material claddings. Figure 3a shows a 3D schematic of a

https://dx.doi.org/10.1021/acssensors.0c00180
ACS Sens. 2020, 5, 861−869

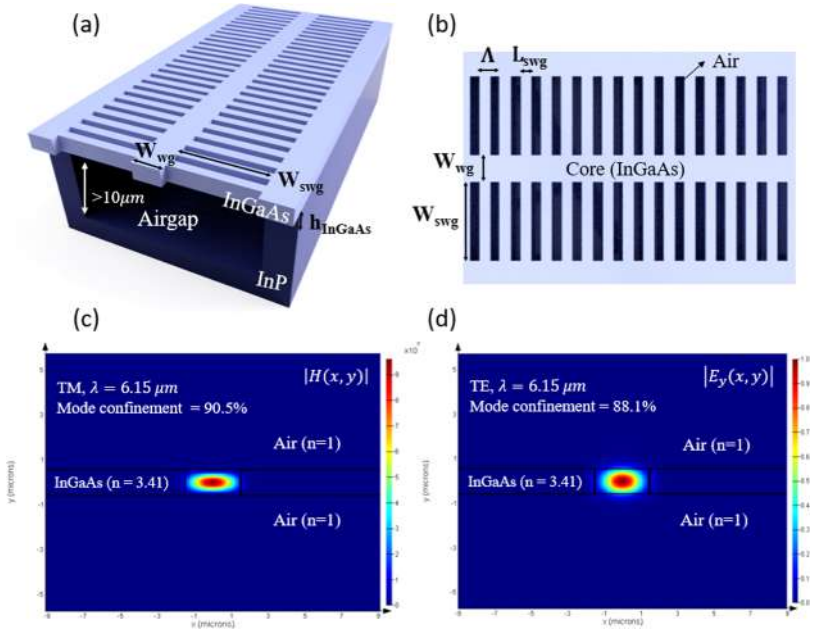

Figure 3. (a) 3D schematic of suspended InGaAs SWW structure. (b) Top-view schematics of suspended InGaAs SWW. (c) Cross section of the fundamental TM mode profile. (d) TE mode profile at λ = 6.15 μm.

suspended InGaAs SWW structure, and Figure 3b shows the top-view schematics. The lateral SWG claddings have an effective refractive index intermediate between the indices of InGaAs and air based on the effective medium theory (EMT)[32]

$$n_{\mathrm{TE}}{}^{2} = n_1{}^{2}f + n_2{}^{2}(1-f) \text{ and}$$
$$n_{\mathrm{TM}}{}^{-2} = n_1{}^{-2}f + n_2{}^{-2}(1-f) \quad (1)$$

where $f = L_{\mathrm{swg}}/\Lambda$ is the volume fraction of the material with index n_1. In addition, they allow easy access of the wet etchant for the removal of the underlying InP cladding, as well as support for the InGaAs strip waveguide after being suspended. Light is index-guided in the InGaAs strip waveguide surrounded by the upper/lower air claddings and the lateral SWG claddings, and the structural slow light is generated by modulating the index-guided optical mode with SWG sidewalls along the propagation direction.[34,35] Additionally, the propagating mode can interact with ammonia gas not only in the upper air cladding but also in the lower air claddings and lateral SWG air holes, so it can effectively enhance the sensitivity through increasing the percentage of mode overlap with the analyte.

We optimized the lattice periodicity of SWG claddings to suppress reflection and diffraction effects and operate in the subwavelength regime by choosing a lattice periodicity that is less than half the Bragg period (eq 2) using the Bloch−Floquet formalism.[32]

$$\Lambda < \frac{1}{2}\frac{\lambda}{n_{\mathrm{B}}} \quad (2)$$

Since the lateral SWG claddings cause the lateral leakage, duty cycle (L_{swg}/Λ) determines the mode confinement in the core waveguide; as duty cycle increases, the effective refractive index contrast between the InGaAs core waveguide and the SWG claddings ($\Delta n = n_{\mathrm{InGaAs}} - n_{\mathrm{swg}}$) decreases, which makes the lateral mode leakage bigger and induces higher propagation loss.[14−17] However, if the duty cycle is too low, L_{swg} is not thick enough to support complete suspension of the membrane. We optimized the duty cycle to minimize the lateral leakage as well as to ensure the structure's mechanical stability.

Moreover, an appropriate SWG width (W_{SWG}) is determined to provide sufficiently wide holes for sacrificial wet etching but with enough material intact to prevent the structure from collapsing after suspending it. Table 1 shows the optimized dimensions of the suspended SWW device for the fundamental TM mode at λ = 6.15 μm.

Table 1. Designed Dimensions of the Suspended InGaAs SWW Device at λ = 6.15 μm

W_{wg}	3 μm	L_{SWG}	575 nm
W_{SWG}	10 μm	Λ	1150 nm
h_{InGaAs}	1.15 μm	t_{air}	>10 μm

Figure 3c,d shows the mode simulations of the fundamental TM and TE modes at λ = 6.15 μm, respectively. Due to the high-index contrast between the strip waveguide and the claddings, the SWW exhibits sufficient mode confinement to reduce the propagation loss. Moreover, both fundamental TM and TE modes are supported with 90.5 and 88.1% mode confinement in the waveguide, respectively. Figure S4 shows the group index of suspended SWW with optimized dimensions with n_{g} = 14.8 at λ = 6.15 μm. Furthermore, we carried out a finite-difference time-domain (FDTD) simulation to see the electromagnetic field propagating in the actual SWW structure. Figure S5e,f shows the top and side views of the fundamental TM mode propagation in the SWW, and Figure S5g shows the TM mode profile in the cross section of SWW, which is well matched with Figure 3c. The percentage of mode overlap with the analyte is approximately 10%.

Next, we fabricated both HPCW and SWW devices and experimentally measured the propagation loss and compared their gas sensing performances.

https://dx.doi.org/10.1021/acssensors.0c00180
ACS Sens. 2020, 5, 861−869

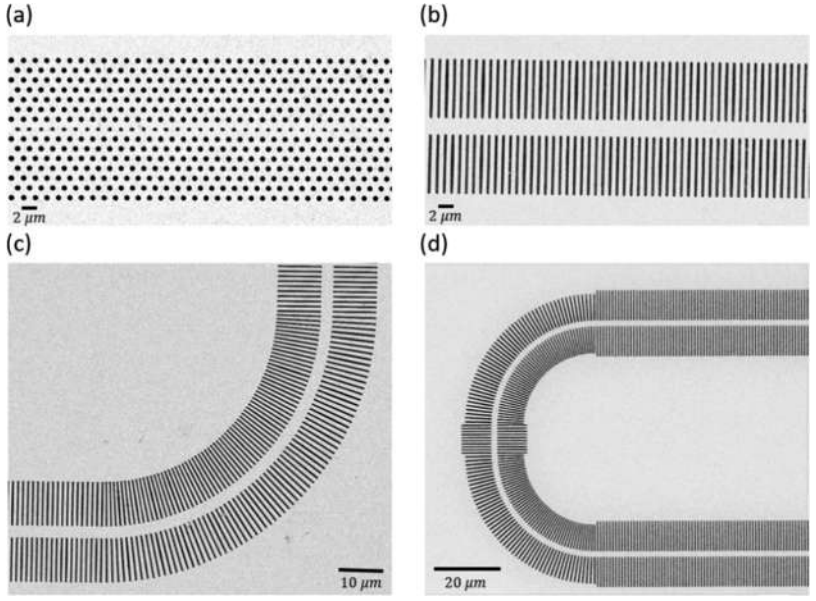

Figure 4. SEM images of the fabricated suspended InGaAs waveguides. (a) Top view of suspended HPCWs. (b) Top view of suspended SWWs. (c) 90° bend structure with 50 μm bend radius. (d) 180° bend structure with 30 μm bend radius.

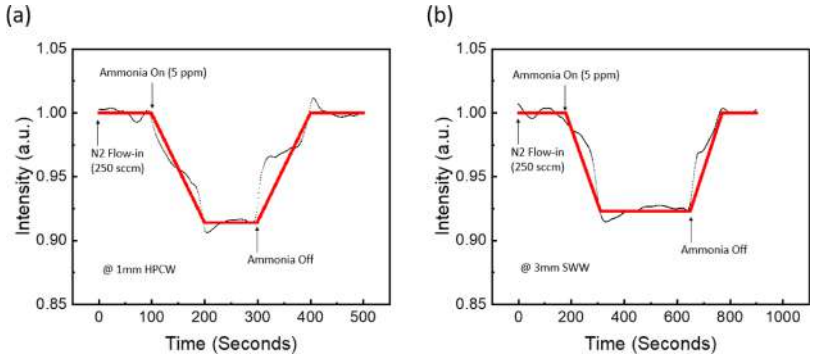

Figure 5. Ammonia sensing results. (a) 1 mm long HPCW device ammonia detection result at 5 ppm with TE polarized light. (b) 3 mm long SWW device ammonia detection result at 5 ppm with TM polarized light.

RESULTS AND DISCUSSION

Since the whole fabrication process is the same for HPCW and SWW devices, we utilize one wafer to fabricate both HPCWs and SWWs. Figure 4 shows scanning electron microscopy (SEM) images of a fabricated device. Figure 4a,b shows top views of the suspended HPCWs and SWWs, respectively. Figure 4c,d shows 90° bend with 50 μm bend radius and 180° bend with 30 μm bend radius, respectively. Cross-sectional SEM images of each device can be found in Figure S1 (inset) and in Figure 1a,b. We can see that the waveguide membranes are fully suspended without upper or lower cladding, and the air gap depth under the waveguides is more than 20 μm, which is enough to avoid mode penetration to the substrate. Despite this considerably deep undercut etch, top-view and cross-sectional SEMs indicate robustness of suspended InGaAs structures showing no sag or bends even after cleaving.

Measurement Results. By measuring the output power versus time, in the presence and absence of ammonia flow from a calibrated Kintek vapor generator, we could evaluate the ammonia sensing performances of HPCWs and SWWs. We experimentally measured the background noise level of ~0.09 dB, which is equivalent to ~2% output signal changes in our measurement setup. We also measured the propagation losses of both the suspended HPCW and the SWW by the cutback method as 39.1 and 4.1 dB/cm, respectively.

Figure 5a shows the ammonia sensing result using 1 mm long HPCW device with TE polarized light. At t = 0, only 250 sccm carrier nitrogen (N_2) gas flows on the chip. At t = 120 s, when 5 ppm calibrated ammonia gas is turned on, an 8.6% signal drop is measured in the output signal. When ammonia is turned off at t = 300 s, but the carrier gas is still flowing, the transmission level goes back to the t = 0 level. Here, Figure 5b shows the ammonia sensing result using a 3 mm long SWW device with TM polarized light. At t = 0, ammonia gas is absent, same as Figure 5a, then 5 ppm calibrated ammonia gas is turned on at t = 180 s, and a 7.7% signal drop is measured. These results indicate that both the 1 mm HPCW and 3 mm SWW devices are capable of performing 5 ppm ammonia gas sensing. The slopes observed during ammonia on/off are related to the lag time of ammonia flow from the vapor generator via tubing to the surface of our chip, which in turn is related to the flow rate of the carrier N_2. Note that this flow rate also determines the effective concentration of ammonia gas, and so is set for this purpose.

Discussion. Table 2 shows the overall comparison between SWWs and HPCWs. The most important difference between

https://dx.doi.org/10.1021/acssensors.0c00180
ACS Sens. 2020, 5, 861−869

Table 2. Comparison between HPCWs and SWWs

waveguide type		HPCW	SWW
optical properties	TE/TM mode guiding	only TE mode	both modes
	group index (n_g)	39	15
	overlap factor	12%	10%
ammonia sensing measurement[a]	signal drop (@ 5 ppm)	8.6%	7.7%
	propagation loss	39.1 dB/cm	4.1 dB/cm
QCL/QCD integrated circuits[b]	polarization rotator (P.R.)	required	N/A
	passive device total length (waveguide + P.R.)	4.86 mm + 40 mm* (*P.R. length)	9 mm
	minimum sensing sensitivity	232 ppb	84 ppb

[a]Experimental data using 1 mm suspended HPCWs and 3 mm suspended SWWs. [b]Estimated specification of monolithic integrated sensors based on the performances of discrete components.

HPCW and SWW is that HPCW can effectively reduce the optical absorption path length due to the high group index value, but it has much higher propagation loss. Based on Beer–Lambert infrared absorption spectroscopy, transmitted intensity I is given by

$$\frac{I}{I_0} = \exp(-\alpha\gamma LC) \tag{3}$$

where I_0 is the incident intensity, α is the absorption coefficient of the medium, L is the optical path length, C is the ammonia gas concentration, and γ is the medium-specific absorption factor determined by dispersion-enhanced light–matter interaction. γ is given by perturbation theory as[41]

$$\gamma = f \times \frac{c/n}{v_g} \tag{4}$$

where c is the velocity of light in free space, v_g is the group velocity in medium of effective index n, and f is the overlap factor denoting the relative fraction of optical field residing in the analyte medium. Using eqs 3 and 4 with the data in Table 2, we can calculate that $\frac{\gamma_{HPCW}}{\gamma_{SWW}} = 3.19$ so that the signal drop of 1 mm HPCW in the presence of 5 ppm ammonia should be 1.06 times as large as that of 3 mm SWW. We experimentally measured a 1.12 times larger signal drop in a 1 mm HPCW in comparison to a 3 mm SWW, matching well with the theoretical value. As a result, with the same device length, the suspended HPCW is about 3 times as sensitive as the SWW by virtue of the slow-light effect. However, other significant advantages of SWWs against HPCW uphold the SWW as a substantial device.

Since we are considering monolithic integrated gas sensors with QCL/QCDs, the total transmitted light intensity detected from a QCD (I_{QCD}) in a monolithic integrated system can be calculated by

$$\begin{aligned} I_{QCD} = I_{QCL} &\times (\text{total polarization rotator loss}) \\ &\times (\text{total coupling loss}) \times (\text{total bend loss}) \\ &\times (\text{total waveguide propagation loss}) \\ &\times \exp(-\alpha\gamma LC) \end{aligned} \tag{5}$$

where I_{QCL} is the QCL output light intensity. Here, we experimentally measured the propagation loss of the HPCW at about 9.5 times $\left(\frac{39.1\text{ dB / cm}}{4.1\text{ dB / cm}}\right)$ as high as that of the SWW. In addition, since HPCW can guide only TE mode, two polarization rotators are required to utilize TM polarized-characteristic QCL/QCD devices. Overall, incorporating an HPCW into an integrated system makes the total transmission loss even higher, which is a significant constraint in the design of extended lengths of waveguide in integrated circuits and may hinder the improvement of the gas sensing sensitivities.

On the other hand, the significantly lower propagation loss of suspended SWW devices permits longer waveguides and in turn higher gas sensing sensitivities. Another important advantage of SWWs is that they can support both TE and TM polarized light. This eliminates the need for polarization rotator devices, reducing both the overall transmission loss (eq 5) and the fully integrated device's footprint, and it also alleviates the complexity of the full fabrication process. Furthermore, in contrast to HPCWs where any bend in the waveguide induces significant bending loss, compact 90° bends with down to 20 μm bend radius have less than 0.2 dB bending loss in SWWs,[38] enabling the use of wraparound waveguides (folded to run back and forth) to reduce the length of the device's footprint and make more efficient use of chip area. Besides, the use of SWWs also avoids the coupling insertion losses typical in well-compensated PCW structures due to group velocity mismatch between regular strip waveguides and PCWs.

In Table 2, we estimated the specification of monolithic integrated sensors based on the performance of discrete components that we have analyzed so far. We estimate 232 ppb sensing sensitivity from a 4.86 mm long HPCW, but with the two 2 cm polarization rotators required for its incorporation,[36] the total passive device length becomes 44.86 mm, as we can see in Figure S7a. On the other hand, an 84 ppb sensing sensitivity can be achieved by a 44.9 mm long SWW, but with a wraparound waveguide consisting of eight 90° bends, the length of the device's footprint can be reduced to 9 mm, as shown in Figure S7b. The detailed explanation of the total transmission loss and the minimum sensitivity calculation is described in the Supporting Information. In addition, the minimum sensing sensitivity can be further improved by eliminating various sources of background noise from the measurement setup, such as the vibration from the pump in the adjacent lab, unavoidable air-conditioning facilities in the lab. Without these extra noise sources, a higher signal-to-noise ratio (SNR) can be achieved, and, in turn, a better sensing sensitivity is anticipated.

In conclusion, we assert that the suspended SWW structure in the InGaAs/InP platform is more favorable for ultimate use in monolithic integrated circuits due to its higher sensitivity with smaller device footprint along with a mitigated complexity of the full fabrication process.

CONCLUSIONS

We have designed, fabricated, and characterized suspended InGaAs HPCWs and SWWs using the InGaAs–InP platform at a wavelength of 6.15 μm for ammonia sensing. We experimentally detected 5 ppm ammonia from 1 mm long suspended InGaAs HPCWs and 3 mm long suspended InGaAs SWWs, which demonstrates that an almost same gas sensing sensitivity of HPCWs can be achievable with ~3 times longer

https://dx.doi.org/10.1021/acssensors.0c00180
ACS Sens. 2020, 5, 861–869

SWWs. We also measured the propagation loss of each device: 39.1 and 4.1 dB/cm for HPCWs and SWWs, respectively. Furthermore, based on the Beer–Lambert infrared absorption law and the experimental results of discrete components, we estimated the minimum detectable gas concentration of 84 ppb from a QCL/QCD integrated SWW sensor. In combination with our other studies into the monolithic integration of QCL/QCDs and passive waveguiding devices, this study contributes to the technological base required for a future integrated-on-chip absorption spectrometer. Our future work will include refining the fabrication process to reduce surface roughness and in turn the propagation loss and applying the same approach to detecting other gases. Finally, monolithically integrated gas sensing circuits will be presented, and we expect this on-chip mid-IR photonic waveguide gas sensing platform with lower cost will open a plethora of applications.

METHODS

Mode Profile and Photonic Band Structure Simulation. The waveguide simulations were performed using the finite-difference eigenmode (FDE) solver in Lumerical Mode Solutions software and the Rsoft band-solver to characterize the mode profile and band gap properties. We can achieve dispersion diagrams of the PCW and extract the group index, stop gap, and bandwidth values from dispersion diagram. Also, the software provides the function of visualizing 3D electrical field profile. The effective refractive indices of the SWW components calculated based on eq 1 for the TM mode are: n_{InGaAs} = 3.41 for the InGaAs core, n_{swg} = 1.36 for the lateral SWG claddings, and n_{air} = 1 for upper/lower air claddings. The FDTD simulation of the SWW was done by Lumerical FDTD software. We set the single fundamental TM mode source at the tip of the SWW structure and placed monitors to see the cross section, as well as top and side views of beam propagation.

Fabrication of Suspended InGaAs HPCW and SWW. First of all, epitaxial growth of InP/InGaAs/InP/InGaAs layers on InP substrate wafers was performed by OEpic company (Figure S6a). The layers are designed for monolithic integration with QCL/QCD and PRS devices at λ = 6.15 μm[38,39] as shown in Figure S1. We defined suspending area using contact photolithography with AZ 5214-E photoresist (PR) (Figure S6b). Once defined, we etched away the top three layers with a series of selective wet etches. $H_2SO_4/H_2O_2/H_2O$ = 1:1:50 solution and HCL/H_2O = 2:1 solution were used for etching InGaAs and InP layers, respectively (Figure S6c). Then, we deposited ~70 nm gold alignment markers to align waveguides with the defined area. Once the global cross-alignment markers are deposited, the hard mask layer of ~250 nm SiO_2 is deposited, and we spin-coat the sample with ~500 nm ZEP-520A resist and pattern the waveguides on it using Jeol FSE 6000 e-beam lithography (Figure S6d). Next, the exposed SiO_2 and III–V layers are etched in sequence, using a reactive-ion etcher (Plasma-Therm 790 RIE) with CHF_3/O_2 gases for oxide etching, and inductively coupled plasma (Oxford 100 ICP) etcher with $Cl_2/Ar/N_2$ gases for III–V etching (Figure S6e). After removing the remaining PR and oxide using an O_2 plasma asher and buffered oxide etch (BOE), the suspending area is defined by PR once more for suspending the HPCW and SWW structures using photolithography (Figure S6f). Then, the sample was immersed in a HCL/H_2O = 4:1 solution at room temperature for 2.5 min, which facilitates the complete removal of the lower InP cladding with a >20 μm etching depth (Figure S6g).

Measurements and Instrumentation. The waveguides are cleaved at the ends and characterized with an end-fire coupling setup as shown in Figure S8. The measurement setup employed an external single-mode continuous-wave distributed-feedback QCL (Thorlabs QD6500CM1) capable of emitting light with a maximum output power of 40 mW and wavelength of 6.15 μm. The emitted light is collimated through a black diamond-2 lens with a focal length of 1.8 mm, and a wire-grid polarizer (WGP) and half-wave plate (HWP) were used to rotate the input polarization from TM to TE or vice versa, before coupling into the waveguides. A chopper wheel connected to lock-in-amplifier modulated the light, and another black diamond-2 lens with a focal length of 1.6 cm was used to focus the light onto the cleaved facet of the waveguides. The input optical power focused to the input facet is 1.38 mW. The light is coupled into the waveguides using end-fire coupling, and the output light from the output facet is coupled into a multimode As_2Se_3 fiber (IRflex IRF-Se-300). The fiber guides the output light to a liquid-nitrogen-cooled HgCdTe detector (Kolmar Technologies, Inc., KMPCP14-1-J1), which is connected to a lock-in-amplifier to improve the SNR. Ammonia gas which is released from the Kintek vapor generator at a certain concentration is delivered via tubing directly to the surface of the chip. Figure S9 shows a photo of the measurement setup.

ASSOCIATED CONTENT

Supporting Information

The Supporting Information is available free of charge at https://pubs.acs.org/doi/10.1021/acssensors.0c00180.

Schematic illustration of an envisioned monolithic integrated circuits with QCL/QCDs and waveguide devices; information on the previous studies regarding monolithic integration of discrete components; mode simulations of the unsuspended and suspended InGaAs HPCWs; the group index versus wavelength of the optimized HPCW and SWW; FDTD simulation results of optimized SWW; fabrication process illustration; a comparison between the conventional strip waveguide and the suspended HPCW and SWW in the same InGaAs/InP platform; the detailed description of the minimum sensitivity calculation; schematic illustration and the picture of measurement setup; and extra SEM and optical microscopy images of SWW devices with various bend structures (PDF)

AUTHOR INFORMATION

Corresponding Author

Ray T. Chen – *Department of Electrical and Computer Engineering, The University of Texas at Austin, Austin, Texas 78758, United States; Omega Optics Inc., Austin, Texas 78757, United States*; Email: chenrt@austin.utexas.edu

Authors

Kyoung Min Yoo – *Department of Electrical and Computer Engineering, The University of Texas at Austin, Austin, Texas 78758, United States*; orcid.org/0000-0002-0928-6952

Jason Midkiff – *Department of Electrical and Computer Engineering, The University of Texas at Austin, Austin, Texas 78758, United States*

Ali Rostamian – *Department of Electrical and Computer Engineering, The University of Texas at Austin, Austin, Texas 78758, United States*

Chi-jui Chung – *Department of Electrical and Computer Engineering, The University of Texas at Austin, Austin, Texas 78758, United States*

Hamed Dalir – *Omega Optics Inc., Austin, Texas 78757, United States*

Complete contact information is available at: https://pubs.acs.org/10.1021/acssensors.0c00180

Notes

The authors declare no competing financial interest.

https://dx.doi.org/10.1021/acssensors.0c00180
ACS Sens. 2020, 5, 861–869

■ ACKNOWLEDGMENTS

The authors appreciate the significant contribution of Dr S. Chakravarty and also wish to thank the anonymous reviewers for their valuable suggestions. The research was supported by Army (ARO) SBIR Contract #W911NF-18-C-0085 and Dr M. Gerhold. Also, the initial simulations were supported by NSF Award #1932753. The content of the information does not necessarily reflect the position or the policy of the Government, and no official endorsement should be inferred.

■ REFERENCES

(1) Yadav, L. D. S. *Organic Spectroscopy*; Kluwer: Boston, 2005; pp 1−324.
(2) Timmer, B.; Olthuis, W.; van den Berg, A. Ammonia Sensors and Their Applications - A Review. *Sens. Actuators, B* **2005**, *107*, 666−677.
(3) Thorpe, M. J.; Moll, K. D.; Jones, R. J.; Safdi, B.; Ye, J. Broadband Cavity Ringdown Spectroscopy for Sensitive and Rapid Molecular Detection. *Science* **2006**, *311*, 1595−1599.
(4) Lackner, M. Tunable Diode Laser Absorption Spectroscopy (TDLAS) in The Process Industries - A Review. *Rev. Chem. Eng.* **2007**, *23*, 65−147.
(5) Ma, Y. F.; Yu, G.; Zhang, J. B.; Yu, X.; Sun, R.; Tittel, F. K. Quartz Enhanced Photoacoustic Spectroscopy Based Trace Gas Sensors Using Different Quartz Tuning Forks. *Sensors* **2015**, *15*, 7596−7604.
(6) Zou, Y.; Chakravarty, S.; Chung, C. J.; Xu, X. C.; Chen, R. T. Mid-infrared Silicon Photonic Waveguides and Devices [Invited]. *Photonics Res.* **2018**, *6*, 254−276.
(7) Schwarz, B.; Ristanic, D.; Reininger, P.; Zederbauer, T.; MacFarland, D.; Detz, H.; Andrews, A. M.; Schrenk, W.; Strasser, G. High Performance Bi-Functional Quantum Cascade Laser and Detector. *Appl. Phys. Lett.* **2015**, *107*, No. 071104.
(8) Zou, Y.; Vijayraghavan, K.; Wray, P.; Chakravarty, S.; Belkin, M. A.; Chen, R. T. Monolithically Integrated Quantum Cascade Lasers, Detectors and Dielectric Waveguides at 9.5 mu m for Far-Infrared Lab-on-Chip Chemical Sensing. *Conf. Lasers Electro-Opt.* **2015**, DOI: 10.1364/CLEO_SI.2015.STu4I.2.
(9) Yao, Y.; Hoffman, A. J.; Gmachl, C. F. Mid-Infrared Quantum Cascade Lasers. *Nat. Photonics* **2012**, *6*, 432−439.
(10) Wolf, J. M.; Riedi, S.; Suess, M. J.; Beck, M.; Faist, J. 3.36 mu m Single-Mode Quantum Cascade Laser with A Dissipation Below 250 mW. *Opt. Express* **2016**, *24*, 662−671.
(11) Kitamura, R.; Pilon, L.; Jonasz, M. Optical Constants of Silica Glass from Extreme Ultraviolet to Far Infrared at Near Room Temperature. *Appl. Opt.* **2007**, *46*, 8118−8133.
(12) Soref, R. Mid-Infrared Photonics in Silicon and Germanium. *Nat. Photonics* **2010**, *4*, 495−497.
(13) Nedeljkovic, M.; Penades, J. S.; Mittal, V.; Murugan, G. S.; Khokhar, A. Z.; Littlejohns, C.; Carpenter, L. G.; Gawith, C. B. E.; Wilkinson, J. S.; Mashanovich, G. Z. Germanium-on-Silicon Waveguides Operating at Mid-Infrared Wavelengths up to 8.5 mu m. *Opt. Express* **2017**, *25*, 27431−27441.
(14) Osman, A.; Nedeljkovic, M.; Penades, J. S.; Wu, Y.; Qu, Z.; Khokhar, A. Z.; Debnath, K.; Mashanovich, G. Z. Suspended Low-Loss Germanium Waveguides for The Longwave Infrared. *Opt. Lett.* **2018**, *43*, 5997−6000.
(15) Penadés, J. S.; Sanchez-Postigo, A.; Nedeljkovic, M.; Ortega-Monux, A.; Wanguemert-Perez, J. G.; Xu, Y.; Halir, R.; Qu, Z.; Khokhar, A. Z.; Osman, A.; et al. Suspended Silicon Waveguides for Long-Wave Infrared Wavelengths. *Opt. Lett.* **2018**, *43*, 795−798.
(16) Penades, J. S.; Ortega-Monux, A.; Nedeljkovic, M.; Wanguemert-Perez, J. G.; Halir, R.; Khokhar, A. Z.; Alonso-Ramos, C.; Qu, Z.; Molina-Fernandez, I.; Cheben, P.; et al. Suspended Silicon Mid-Infrared Waveguide Devices with Subwavelength Grating Metamaterial Cladding. *Opt. Express* **2016**, *24*, 22908−22916.
(17) Penadés, J. S.; Alonso-Ramos, C.; Khokhar, A. Z.; Nedeljkovic, M.; Boodhoo, L. A.; Ortega-Monux, A.; Molina-Fernandez, I.; Cheben, P.; Mashanovich, G. Z. Suspended SOI Waveguide with Sub-Wavelength Grating Cladding for Mid-Infrared. *Opt. Lett.* **2014**, *39*, 5661−5664.
(18) Bi, W.; Li, A. The Dispersion of The Refractive Index of III-V Semiconductors. *J. Appl. Phys.* **1992**, *71*, 2826−2829.
(19) Gilles, C.; Orbe, L. J.; Carpintero, G.; Maisons, G.; Carras, M. Mid-Infrared Wavelength Multiplexer in InGaAs/InP Waveguides Using a Rowland Circle Grating. *Opt. Express* **2015**, *23*, 20288−20296.
(20) Charlton, C.; Giovannini, M.; Faist, J.; Mizaikoff, B. Fabrication and Characterization of Molecular Beam Epitaxy Grown Thin-Film GaAs Waveguides for Mid-Infrared Evanescent Field Chemical Sensing. *Anal. Chem.* **2006**, *78*, 4224−4227.
(21) Jung, S.; Palaferri, D.; Zhang, K.; Xie, F.; Okuno, Y.; Pinzone, C.; Lascola, K.; Belkin, M. A. Homogeneous Photonic Integration of Mid-Infrared Quantum Cascade Lasers with Low-Loss Passive Waveguides on an InP Platform. *Optica* **2019**, *6*, 1023−1030.
(22) Palik, E. D.; Ghosh, G. *Handbook of Optical Constants of Solids*; Academic Press: San Diego, 1998.
(23) Adachi, S. Model Dielectric Constants of GaP, GaAs, GaSb, InP, InAs, and InSb. *Phys. Rev. B* **1987**, *35*, 7454−7463.
(24) Peng, L. H.; Broekaert, T.; Choi, W. Y.; Fonstad, C.; Jones, V. Defect Activated Infrared Multiphonon Excitation in Iron-Doped Semi-Insulating Indium Phosphide. *Appl. Phys. Lett.* **1991**, *59*, 564−566.
(25) Liang, D.; Fang, A.; Oakley, D.; Napoleone, A.; Chapman, D.; Chen, C.-L.; Juodawlkis, P.; Raday, O.; Bowers, J. E. 150 mm InP-to-Silicon Direct Wafer Bonding for Silicon Photonic Integrated Circuits. *ECS Trans.* **2008**, *16*, 235−241.
(26) Lai, W. C.; Chakravarty, S.; Zou, Y.; Chen, R. T. Multiplexed Detection of Xylene and Trichloroethylene in Water by Photonic Crystal Absorption Spectroscopy. *Opt. Lett.* **2013**, *38*, 3799−3802.
(27) Lai, W. C.; Chakravarty, S.; Wang, X. L.; Lin, C. Y.; Chen, R. T. Photonic Crystal Slot Waveguide Absorption Spectrometer for On-Chip Near-Infrared Spectroscopy of Xylene in Water. *Appl. Phys. Lett.* **2011**, *98*, No. 023304.
(28) Lai, W. C.; Chakravarty, S.; Wang, X. L.; Lin, C. Y.; Chen, R. T. On-Chip Methane Sensing by Near-IR Absorption Signatures in A Photonic Crystal Slot Waveguide. *Opt. Lett.* **2011**, *36*, 984−986.
(29) Zou, Y.; Chakravarty, S.; Wray, P.; Chen, R. T. Mid-Infrared Holey and Slotted Photonic Crystal Waveguides in Silicon-on-Sapphire for Chemical Warfare Simulant Detection. *Sens. Actuators, B* **2015**, *221*, 1094−1103.
(30) Ek, S.; Lunnemann, P.; Chen, Y.; Semenova, E.; Yvind, K.; Mork, J. Slow-Light-Enhanced Gain in Active Photonic Crystal Waveguides. *Nat. Commun.* **2014**, *5*, No. 5039.
(31) Zou, Y.; Chakravarty, S.; Wray, P.; Chen, R. T. Experimental Demonstration of Propagation Characteristics of Mid-Infrared Photonic Crystal Waveguides in Silicon-on-Sapphire. *Opt. Express* **2015**, *23*, 6965−6975.
(32) Halir, R.; Bock, P. J.; Cheben, P.; Ortega-Monux, A.; Alonso-Ramos, C.; Schmid, J. H.; Lapointe, J.; Xu, D. X.; Wanguemert-Perez, J. G.; Molina-Fernandez, I.; et al. Waveguide Sub-Wavelength Structures: A Review of Principles and Applications. *Laser Photonics Rev.* **2015**, *9*, 25−49.
(33) Schmid, J. H.; Cheben, P.; Bock, P. J.; Halir, R.; Lapointe, J.; Janz, S.; Delage, A.; Densmore, A.; Fedeli, J.; Hall, T. J.; et al. Refractive Index Engineering With Subwavelength Gratings in Silicon Microphotonic Waveguides. *IEEE Photonics J.* **2011**, *3*, 597−607.
(34) Wang, J.; Ashrafi, R.; Adams, R.; Glesk, I.; Gasulla, I.; Capmany, J.; Chen, L. R. Subwavelength Grating Enabled On-Chip Ultra-Compact Optical True Time Delay Line. *Sci. Rep.* **2016**, *6*, No. 30235.
(35) Chung, C.-J.; Xu, X.; Wang, G.; Pan, Z.; Chen, R. T. On-Chip Optical True Time Delay Lines Featuring One-Dimensional Fishbone Photonic Crystal Waveguide. *Appl. Phys. Lett.* **2018**, *112*, No. 071104.
(36) Chung, C. J.; Midkiff, J.; Yoo, K. M.; Rostamian, A.; Guo, J.; Chen, R. T.; Chakravarty, S. InP-Based Polarization Rotator-Splitter

for Mid-Infrared Photonic Integration Circuits. *AIP Adv.* **2019**, *9*, No. 015303.
(37) Chakravarty, S.; Midkiff, J.; Rostamian, A.; Guo, J.; Chen, R. T. In *Monolithic Integration of Quantum Cascade Laser, Quantum Cascade Detector and Slotted Photonic Crystal Waveguide for Absorbance Sensing from λ = 3−15 μm*, 2018 Conference on Lasers and Electro-Optics (CLEO), 13−18 May, 2018; pp 1−2.
(38) Chakravarty, S.; Midkiff, J.; Yoo, K.; Chung, C. J.; Rostamian, A.; Chen, R. T. Compact Integrated Photonic Components for Lambda = 3−15 micron. *Proc. SPIE 10921, Integrated Optics: Devices, Materials, and Technologies XXIII*, 2019, 109210D, DOI: 10.1117/12.2508885.
(39) Chakravarty, S.; Midkiff, J.; Yoo, K.; Rostamian, A.; Chen, R. T. *Monolithic Integration of Quantum Cascade Laser, Quantum Cascade Detector, and Subwavelength Waveguides for Mid-Infrared Integrated Gas Sensing*; SPIE, 2019; Vol. *10926*.
(40) Yoo, K. M.; Midkiff, J.; Rostamian, A.; Chakravarty, S.; Chen, R. T. In *Suspended Membrane InGaAs Photonic Crystal Waveguides for Ammonia Sensing at λ = 6.15 μm*, 2019 Conference on Lasers and Electro-Optics (CLEO), 5−10 May, 2019; pp 1−2.
(41) Mortensen, N. A.; Xiao, S. Slow-Light Enhancement of Beer-Lambert-Bouguer Absorption. *Appl. Phys. Lett.* **2007**, *90*, No. 141108.

https://dx.doi.org/10.1021/acssensors.0c00180
ACS Sens. 2020, 5, 861−869